J. Fluid Mech. (2019), *vol.* 874, *pp.* 1096–1114.
doi:10.1017/jfm.2019.470

Data-driven construction of a reduced-order model for supersonic boundary layer transition

Ming Yu[1], **Wei-Xi Huang**[1] **and Chun-Xiao Xu**[1,†]

[1]Key Laboratory of Applied Mechanics (AML), Department of Engineering Mechanics, Tsinghua University, Beijing 100084, PR China

(Received 19 September 2018; revised 7 June 2019; accepted 8 June 2019; first published online 15 July 2019)

In this study, a data-driven method for the construction of a reduced-order model (ROM) for complex flows is proposed. The method uses the proper orthogonal decomposition (POD) modes as the orthogonal basis and the dynamic mode decomposition method to obtain linear equations for the temporal evolution coefficients of the modes. This method eliminates the need for the governing equations of the flows involved, and therefore saves the effort of deriving the projected equations and proving their consistency, convergence and stability, as required by the conventional Galerkin projection method, which has been successfully applied to incompressible flows but is hard to extend to compressible flows. Using a sparsity-promoting algorithm, the dimensionality of the ROM is further reduced to a minimum. The ROMs of the natural and bypass transitions of supersonic boundary layers at $Ma = 2.25$ are constructed by the proposed data-driven method. The temporal evolution of the POD modes shows good agreement with that obtained by direct numerical simulations in both cases.

Key words: compressible boundary layers, low-dimensional models, transition to turbulence

1. Introduction

Modal decomposition methods, such as proper orthogonal decomposition (POD) and dynamic mode decomposition (DMD), are able to capture the important structures of fluid flows. Based on the resulting spatial modes, a reduced-order model (ROM) can be constructed to estimate the temporal evolution of the flow field. ROM is a powerful tool for exploring the physical mechanisms of complex flows, predicting their behaviour and designing control schemes, by constructing a finite-dimensional dynamical system of the flows (Rowley & Dawson 2017). Recent developments in machine learning-based flow modelling and control also provide a new framework to control complex dynamical systems (Duriez, Brunton & Noack 2017). The motivation of the present research is to construct ROMs for the supersonic boundary layer transition, which involves very complex physical processes and raises many questions concerning transition prediction and control.

The POD–Galerkin method has been successfully applied to construct ROMs for various incompressible flows (Holmes *et al.* 2012). The ordinary differential equations

† Email address for correspondence: xucx@tsinghua.edu.cn

(ODEs) for the temporal evolution of the modal coefficients (henceforth referred to as 'temporal coefficients') are obtained by projecting the governing equations (i.e. momentum equations in this case) onto the POD modes. Solving the resulting ODEs gives the temporal evolution of the POD modes, yielding the reduced-order representation of the flow field. For instance, Smith (2003) and Ilak & Rowley (2008) constructed low-dimensional models of wall-bounded turbulent flows on the basis of conventional POD and balanced POD, respectively, the latter of which is an approximation of the balanced truncation, a standard modal-reduction method used for stable linear input–output systems (Rowley 2005). Lumley & Poje (1997) further applied the POD–Galerkin method to flows with density fluctuations, and studied the variation of coherent structures as a function of Richardson number. Noack, Papas & Monkewitz (2005) discussed the necessity for a pressure-term representation in empirical Galerkin models of incompressible free shear flows and found that, although the magnitude of pressure terms is small, their effects cannot be neglected.

For compressible viscous flows, ROMs are difficult to obtain via the traditional POD–Galerkin method because of the complexity of the governing equations, the presence of fine-scale (sharp boundary layers) and discontinuous features (shocks) in the solutions to these equations and a general lack of an *a priori* stability guarantee for POD–Galerkin ROMs applied to these equations. Rowley, Colonius & Murray (2004) constructed a ROM with the POD–Galerkin method for compressible isentropic flows, in which the energy equation is replaced by an equation for the speed of sound. The ROM accurately predicted a two-dimensional cavity flow during relatively long-term evolution. Taking viscosity into consideration further increases the complexity because the viscosity varies with temperature, which has been neglected in the previous POD–Galerkin methods. The application to compressible viscous flows was further proposed and performed by Gloerfelt (2008). However, the ODEs thus obtained were unstable, leading to the exponential growth of the temporal coefficients.

Although various modifications have been proposed, such as taking into account the viscous dissipation of the truncated higher modes via eddy viscosity, the parameters involved were usually set artificially and empirically. The stability of the ODEs in the ROMs of compressible flows has aroused much research interest, and has been studied thoroughly with rigorous mathematical proofs (Barone *et al.* 2009). Balajewicz, Tezaur & Dowell (2016) proposed that a goal-oriented rotation of the POD basis would improve the stability of the ROM with the POD–Galerkin method. Elsewhere, the boundary conditions and the inner product have also been considered as potential factors leading to instability (Kalashnikova & Barone 2010). It has been proved that the ROM can be stable and weakly convergent with the correct choice of the inner product and boundary conditions (Kalashnikova *et al.* 2014*b*). While the application of the method to laminar subsonic flows at low Reynolds numbers has so far been successful, for nonlinear flows, the stability and convergence are still challenging. Kalashnikova *et al.* (2014*a*) proposed an improved method to construct stable ROMs for compressible flows. The approach delivers stable and accurate ROMs for linear and laminar flow problems, but for nonlinear problems, the convergence is still not satisfactory. Previous studies have indicated that the traditional methods to construct the ROMs are not yet feasible for compressible viscous flows, especially for complex cases such as transition and turbulence.

DMD is a data-driven method for reduced-order representation, which can extract the spatial modes as well as their frequencies and growth rates (Schmid 2010). Because DMD does not require any governing equations, it has been especially widely applied in compressible flows, for example, the reduced-order representation

of near-wall structures in a transitional boundary layer of Mach 0.2 (Sayadi *et al.* 2014), and the pressure distribution near an isolated roughness element inducing a hypersonic boundary layer transition (Subbareddy, Bartkowicz & Candler 2014). Although DMD is a powerful method to construct the ROM, the resulting modes are not orthogonal, which makes it difficult to investigate the interaction between modes. The recursive dynamic mode decomposition (RDMD) method, recently proposed by Noack *et al.* (2016), in which the DMD modes are orthogonalised, offers a way to combine the advantages of the two main modal decomposition methods, i.e. POD and DMD, to obtain the orthogonal flow basis and its temporal evolution.

In this study, we propose a purely data-driven ROM construction method based on the combination of POD, DMD and sparsity-promoting DMD (Jovanović, Schmid & Nichols 2014). The POD is used to obtain the orthogonal basis, DMD to obtain its temporal evolution and sparsity-promoting DMD for dimension truncation. This method does not involve the governing equations and hence is spared the problems arising from their projection (e.g. instability). The method can be easily applied to compressible as well as incompressible flows, overcoming the difficulties encountered by the conventional POD–Galerkin method. In this study, the supersonic boundary layer transitions at Mach number $Ma = 2.25$ are considered, and the ROMs are obtained using the proposed construction method to allow longer-term prediction of the flow fields.

The remainder of this paper is organised as follows. In § 2, the principles of the present ROM construction method are introduced, and the algorithm and dimension truncation technique are described. The method is applied to the natural and bypass transition processes in a supersonic boundary layer at $Ma = 2.25$ in § 3, where the construction of the ROM is shown in detail. Finally, concluding remarks are given in § 4.

2. Data-driven reduced-order model construction

This section describes the new data-driven construction method of a ROM based on the POD and DMD methods. The principles of POD and DMD are briefly summarised in §§ 2.1 and 2.2, respectively, focusing on their application to discrete systems. Then, in § 2.3, the new method is derived by considering the relationship between POD and DMD.

2.1. *Proper orthogonal decomposition of a discrete system*

POD extracts a set of spatial modes based on the energy of the flow structures. For a discrete system, studied either experimentally or by numerical simulations, the flow quantity v of a certain temporal instantaneous (e.g. the ith) flow field can be written as a column vector,

$$\boldsymbol{v}_i = [v_{1i}, v_{2i}, \ldots, v_{ji}, \ldots, v_{Mi}]^{\mathrm{T}}, \tag{2.1}$$

where the components v_{ji} are the values of the quantity at the spatial point j at temporal instant i, and M is the total number of spatial points in the experiment or numerical simulation. The superscript T represents the transpose of the vector or matrix. With a set of data samples at different temporal instants with a constant time interval, the data samples can be written as a matrix,

$$\boldsymbol{V}_N = [\boldsymbol{v}_1, \boldsymbol{v}_2, \ldots, \boldsymbol{v}_N], \tag{2.2}$$

where N is the number of temporal data samples, or columns in matrix $\boldsymbol{V}_N$. Usually, the dimension of the matrix $M \gg N$ for fluid flow problems. We define the energy matrix $\boldsymbol{R}$ as

$$\boldsymbol{R} = \frac{1}{N}\boldsymbol{V}_N\boldsymbol{V}_N^{\mathrm{T}}, \tag{2.3}$$

which is a symmetrical and semi-positive-definite matrix, whose eigenvalues can be obtained by

$$\boldsymbol{R}\boldsymbol{U} = \boldsymbol{U}\boldsymbol{\Sigma}', \tag{2.4}$$

$$\boldsymbol{U} = [\boldsymbol{u_1}, \boldsymbol{u_2}, \ldots, \boldsymbol{u}_N], \tag{2.5}$$

$$\boldsymbol{\Sigma}' = \mathrm{diag}(\sigma_1', \sigma_2', \ldots, \sigma_N'). \tag{2.6}$$

Here the column vectors $\boldsymbol{u}_i$ of the matrix $\boldsymbol{U}$ are the eigenvectors of $\boldsymbol{R}$, referred to as POD modes, and σ_i' in the diagonal matrix $\boldsymbol{\Sigma}'$ is the eigenvalue, identical to the energy of $\boldsymbol{u}_i$. The POD method is equivalent to the singular value decomposition (SVD) of matrix $\boldsymbol{V}_N$ in such a way that

$$\boldsymbol{V}_N = \boldsymbol{U}\boldsymbol{\Sigma}\boldsymbol{V}^{\mathrm{H}}, \tag{2.7}$$

where $\boldsymbol{\Sigma} = \sqrt{N\boldsymbol{\Sigma}'}$ is a diagonal matrix of rank n (usually $n = N$) with non-zero singular values $\{\sigma_1, \ldots, \sigma_n\}$ on its main diagonal, and $\boldsymbol{U}$ and $\boldsymbol{V}$ are matrices with unit and orthogonal columns, i.e.

$$\boldsymbol{U} \in \mathbb{C}^{N\times n}, \quad \boldsymbol{U}^{\mathrm{H}}\boldsymbol{U} = \boldsymbol{I}, \tag{2.8a,b}$$

$$\boldsymbol{V} \in \mathbb{C}^{n\times M}, \quad \boldsymbol{V}^{\mathrm{H}}\boldsymbol{V} = \boldsymbol{I}, \tag{2.9a,b}$$

where the superscript H refers to the Hermitian transpose of the matrix.

2.2. *Dynamic mode decomposition*

The DMD method needs one more temporal realisation of the flow field than POD, and the data samples can be written as two matrices:

$$\boldsymbol{V}_{N1} = [\boldsymbol{v}_0, \boldsymbol{v}_1, \ldots, \boldsymbol{v}_{N-1}], \quad \boldsymbol{V}_{N2} = [\boldsymbol{v}_1, \boldsymbol{v}_2, \ldots, \boldsymbol{v}_N]. \tag{2.10a,b}$$

It is assumed that the constant time interval Δt is small enough that the two matrices can be related by a linear mapping, i.e.

$$\boldsymbol{V}_{N2} = \boldsymbol{A}\boldsymbol{V}_{N1}, \tag{2.11}$$

where $\boldsymbol{A}$ is the evolving matrix of the dynamical system. Matrix $\boldsymbol{A}$ is unknown and can be seriously ill-conditioned if obtained by taking the pseudo-inverse of $\boldsymbol{V}_{N1}$; thus an orthogonal decomposition of $\boldsymbol{V}_{N1}$ is needed to solve the eigenvalue problem correctly. Performing SVD on $\boldsymbol{V}_{N1}$ as shown in (2.7), the linear mapping shown in (2.11) can further be expressed as

$$\boldsymbol{V}_{N2} = \boldsymbol{A}\boldsymbol{U}\boldsymbol{\Sigma}\boldsymbol{V}^{\mathrm{H}}. \tag{2.12}$$

Then the projection of $\boldsymbol{A}$ on the basis $\boldsymbol{U}$ can be expressed as

$$\boldsymbol{A}' = \boldsymbol{U}^{\mathrm{H}}\boldsymbol{A}\boldsymbol{U} = \boldsymbol{U}^{\mathrm{H}}\boldsymbol{V}_{N2}\boldsymbol{V}\boldsymbol{\Sigma}^{-1}. \tag{2.13}$$

Note that $\boldsymbol{A}'$ shares the same eigenvalues as $\boldsymbol{A}$, but its rank is much lower. The eigenvalues μ_i $(i = 1, 2, \ldots, n)$ and eigenvectors $\boldsymbol{w}_i$ of $\boldsymbol{A}'$ are obtained by solving the following eigenvalue problem:

$$\boldsymbol{A}'\boldsymbol{W} = \boldsymbol{W}\boldsymbol{\Lambda}, \tag{2.14}$$

$$\boldsymbol{\Lambda} = \mathrm{diag}(\mu_1, \mu_2, \ldots, \mu_n), \tag{2.15}$$

$$\boldsymbol{W} = [\boldsymbol{w}_1, \boldsymbol{w}_2, \ldots, \boldsymbol{w}_n], \tag{2.16}$$

and the eigenmodes are obtained by

$$\boldsymbol{\Phi} = \boldsymbol{U}\boldsymbol{W}. \tag{2.17}$$

2.3. *Data-driven reduced-order model construction*

The present data-driven ROM construction method uses POD modes as the orthogonal basis and DMD eigenvalues to represent the temporal evolution of the modes. With the POD modes obtained in (2.4), each temporal realisation of the flow field can be expressed as a linear combination of the POD modes,

$$\boldsymbol{v}_0 = \sum_{i=1}^{N} b_i(0)\boldsymbol{u}_i, \quad \boldsymbol{v}_1 = \sum_{i=1}^{N} b_i(\Delta t)\boldsymbol{u}_i, \ldots, \quad \boldsymbol{v}_N = \sum_{i=1}^{N} b_i(N\Delta t)\boldsymbol{u}_i. \tag{2.18a,b}$$

Substituting the above linear expansions into the linear mapping (2.11), we get

$$\boldsymbol{U}\boldsymbol{B}_2 = \boldsymbol{A}\boldsymbol{U}\boldsymbol{B}_1, \tag{2.19}$$

where $\boldsymbol{B}_1$ and $\boldsymbol{B}_2$ are the matrices of the temporally evolving coefficients:

$$\boldsymbol{B}_1 = \begin{bmatrix} b_1(0) & b_1(\Delta t) & \cdots & b_1((N-1)\Delta t) \\ b_2(0) & b_2(\Delta t) & \cdots & b_2((N-1)\Delta t) \\ \vdots & \vdots & \ddots & \vdots \\ b_N(0) & b_N(\Delta t) & \cdots & b_N((N-1)\Delta t) \end{bmatrix}, \tag{2.20}$$

$$\boldsymbol{B}_2 = \begin{bmatrix} b_1(\Delta t) & b_1(2\Delta t) & \cdots & b_1(N\Delta t) \\ b_2(\Delta t) & b_2(2\Delta t) & \cdots & b_2(N\Delta t) \\ \vdots & \vdots & \ddots & \vdots \\ b_N(\Delta t) & b_N(2\Delta t) & \cdots & b_N(N\Delta t) \end{bmatrix}. \tag{2.21}$$

Equation (2.19) can be further written as

$$\boldsymbol{B}_2 = \boldsymbol{U}^{\mathrm{H}}\boldsymbol{A}\boldsymbol{U}\boldsymbol{B}_1 = \boldsymbol{A}'\boldsymbol{B}_1. \tag{2.22}$$

Note that the SVD is used in both methods, as shown in (2.5) and (2.8). Equation (2.22) indicates that the temporally evolving matrix $\boldsymbol{A}'$ is the same as the matrix defined in (2.13) for DMD, which is the projection of the temporally evolving matrix $\boldsymbol{A}$ on the orthogonal basis $\boldsymbol{U}$. In this sense, the POD and DMD modes are equivalent, as the latter are simply linear combinations of the former. The temporal evolution of the POD modes can be obtained via the DMD eigenvalues and eigenvectors in (2.14). As stated in the previous section, the essential step of the POD–Galerkin method is to obtain the matrix of temporal coefficients. However, the projection of

the equations is quite complicated, and is restricted by many factors, including the numerical schemes and boundary conditions. The present data-driven method avoids all of these problems, and the matrix of temporal coefficients can be easily obtained from data samples.

The discrete form of the temporal evolution equation can be expressed as follows:

$$\boldsymbol{b}(t+\Delta t)=\boldsymbol{A}'\boldsymbol{b}(t), \tag{2.23}$$

where

$$\boldsymbol{b}(t+\Delta t)=[b_1(t+\Delta t), b_2(t+\Delta t), \ldots, b_N(t+\Delta t)]^{\mathrm{T}}, \tag{2.24}$$

$$\boldsymbol{b}(t)=[b_1(t), b_2(t), \ldots, b_N(t)]^{\mathrm{T}}. \tag{2.25}$$

With a group of initial values, the temporal coefficients can be obtained via the above linear mapping. If desired, the formula can be further expressed as ODEs, enabling continuous temporal coefficients to be obtained. The eigenvalues and eigenvectors of $\boldsymbol{A}'$ can be calculated by (2.14), and the logarithms of the eigenvalues

$$\boldsymbol{\Xi}=\mathrm{diag}(\ln\mu_1, \ln\mu_2, \ldots, \ln\mu_n)/\Delta t \tag{2.26}$$

are the eigenvalues of the ODEs, representing the frequency and amplification rate of the DMD modes. Therefore,

$$\boldsymbol{A}_c=\boldsymbol{W}^{-1}\boldsymbol{\Xi}\boldsymbol{W} \tag{2.27}$$

is the temporal evolution matrix of the ODEs, i.e.

$$\frac{\mathrm{d}\boldsymbol{b}(t)}{\mathrm{d}t}=\boldsymbol{A}_c\boldsymbol{b}(t), \tag{2.28}$$

which can be solved by classical algorithms such as the Runge–Kutta method.

Because the number of temporal data samples is usually of the order of $O(10^2)$, the dimensionality of the ROM is still high. The sparsity-promoting (SP) dynamic mode decomposition (SPDMD) (Jovanović *et al.* 2014) provides a way to lower its dimensionality. SPDMD addresses the dimension reduction of the full-rank decomposition by adding a penalty function term in the standard optimisation problem. The SP method removes the modes with large damping rates or small amplitudes and leaves only those with strong contributions to the original data sequence. In temporal equilibrium systems, there are no significant damping modes, and the SP method only removes modes with small amplitudes, leaving the important modes needed to construct an appropriate ROM. Because the POD modes are ranked by energy, the dimensionality of the ROM should be larger than, or at least equal to, the number of modes selected by the SP method. Therefore, the truncation of $\boldsymbol{A}'$ can be performed as follows. Assuming that the appropriate number of ROM dimensions is r, and the r POD modes are used and written as $\boldsymbol{U}_r\in\mathbb{R}^{M\times r}$, then we have

$$\boldsymbol{A}_r=\boldsymbol{U}_r^{\mathrm{H}}\boldsymbol{A}\boldsymbol{U}_r=\boldsymbol{U}_r^{\mathrm{H}}\boldsymbol{V}_{N2}\boldsymbol{V}_r\boldsymbol{\Sigma}_r^{-1}, \tag{2.29}$$

where the matrix with subscript r on the right-hand side represents the truncated matrix, leaving the first r rows (for $\boldsymbol{U}^{\mathrm{H}}$), columns (for $\boldsymbol{V}$) or both (for $\boldsymbol{\Sigma}$). Substituting the matrix $\boldsymbol{A}_r$ into (2.28) and using only the first r temporal coefficients $b_1, b_2, \ldots, b_r$, then an r-dimensional ROM can be obtained.

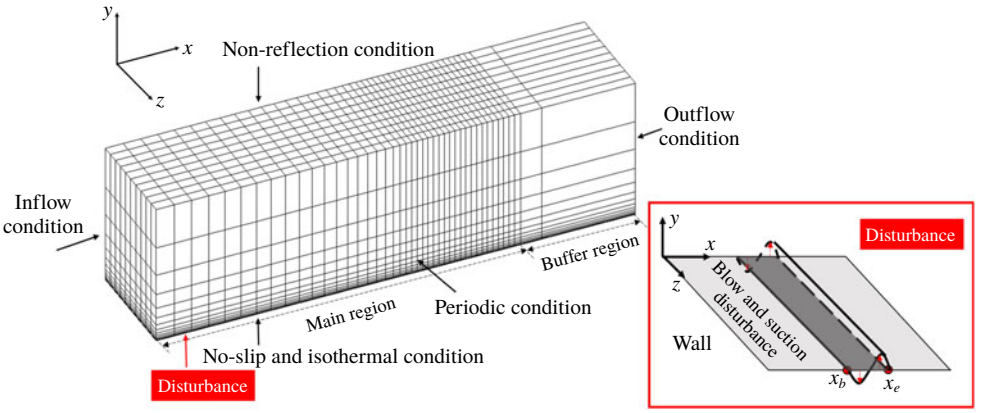

FIGURE 1. (Colour online) Computational configuration.

The ROM construction process is briefly summarised as follows:

(1) Write the data samples (with a constant time interval) obtained by numerical simulations or experimental measurements in the form of matrices $\boldsymbol{V}_{N1}$ and $\boldsymbol{V}_{N2}$ as dictated by (2.10).
(2) Perform SVD via equation (2.7) on the matrix $\boldsymbol{V}_{N1}$ to obtain the orthogonal basis $\boldsymbol{U}$ and the singular values $\boldsymbol{\Sigma}$. The energy of each mode is obtained.
(3) Perform DMD by solving (2.11)–(2.14) and (2.26).
(4) Truncate $\boldsymbol{A}'$ to lower dimensions according to the SPDMD results or the energy of the POD modes according to (2.29), and obtain the temporal evolution matrix from (2.27) by replacing $\boldsymbol{A}_c$ with $\boldsymbol{A}_r$.
(5) Solve (2.28) numerically to give the temporal evolution of the POD modes.

3. Application: reduced-order model for supersonic boundary layer transition

In this section, direct numerical simulation (DNS) is performed to predict the natural and bypass transitions in supersonic boundary layers, where the ROM is built with the above-proposed data-driven method. To evaluate its performance, the temporal coefficients obtained by the ROM are compared with those obtained by the direct projection of the DNS data. The construction of the ROMs is shown step by step in the following to illustrate some important mechanisms found in the results of the intermediate steps.

3.1. *Numerical set-up*

The supersonic boundary layer transition for an ideal gas and a Newtonian fluid is simulated by DNS using OPENCFD-1.10.4, developed by Li *et al.* (2010). The conservative governing equations are solved numerically with the high-order finite difference method. The convection terms are approximated with the seventh-order weighted essentially non-oscillatory (WENO) scheme, and the viscous terms are approximated with the sixth-order central difference scheme. The third-order total variation diminishing (TVD) Runge–Kutta scheme is adopted for time advancement. The details of the numerical schemes and validation of the code can be found in Li *et al.* (2010).

The computational configurations and boundary conditions are shown in figure 1. The computational domain is divided into the main region with a fine mesh and

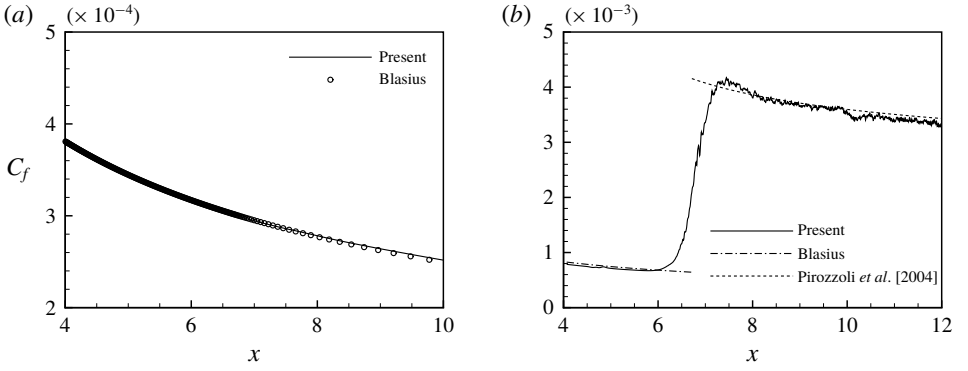

FIGURE 2. Streamwise variation of C_f: (*a*) linear case, and (*b*) nonlinear case.

Cases	Re_∞ (inch^{-1})	Ma_∞	T_∞	T_w/T_∞	Domain $L_x \times L_y \times L_z$	Grid number $N_x \times N_y \times N_z$
Linear	635 000	2.25	169.44	1.9	$12 \times 0.2 \times 0.35$	$340 \times 72 \times 256$
Nonlinear					$15 \times 0.2 \times 0.35$	$2984 \times 72 \times 256$

TABLE 1. Computational parameters.

the buffer region with gradually coarser meshes to minimise the influence of the outlet boundary condition. At the inlet of the computational domain, the laminar profiles of density (ρ), velocity (u, v and w, the velocity components in the x, y and z directions) and temperature (T) are set as those obtained by the two-dimensional numerical simulation with the same parameters and boundary conditions. At the wall, a no-slip condition is adopted for velocities and the isothermal condition for temperature. A non-reflection condition is adopted at the upper boundary, and a periodic condition in the spanwise direction.

For the supersonic boundary layer, the flow parameters are set according to Pirozzoli, Grasso & Gatski (2004), i.e. the free-stream Reynolds number $Re = 635\,000$ inch^{-1}, Mach number $Ma = 2.25$ and temperature 169.0 K. The wall temperature is 1.9 times the free-stream temperature. All of the flow quantities in the following are non-dimensionalised by the reference density, velocity and temperature of the free stream, and the characteristic length is chosen to be 1 inch. Two separate cases are considered, with linear and nonlinear disturbances (inducing natural and bypass transitions, respectively). The computational domain and grid numbers for each case are listed in table 1, in which the subscripts x, y and z denote streamwise, wall-normal and spanwise directions, respectively.

To trigger the transition, a periodic blowing and suction disturbance is introduced at the wall in the region of $x = 4.0$–4.5. The formulation of the disturbance can be found in Pirozzoli *et al.* (2004). The frequencies introduced are 3.982 and 7.854, with spanwise wavenumbers of 35.9 and 71.8 (corresponding to one and two waves in the spanwise direction), which are linearly unstable according to linear stability analysis. In the linear case, the disturbance amplitudes are set to 0.0003 for the two frequencies, and in the nonlinear case both are set to 0.004. The streamwise distributions of the mean skin friction coefficient (C_f) are shown in figure 2 in comparison with that of the

laminar Blasius boundary layer and that of a turbulent flow given by Pirozzoli *et al.* (2004). The C_f values before and after the transition show good agreement with the reference results of laminar and turbulent flows, respectively.

3.2. *Reduced-order model of natural transition*

First, the ROM of the flow with a linear disturbance is built to validate the proposed ROM construction method. The flow quantities used in the analysis are the three velocity components u, v and w, density ρ and temperature T. The mean values are subtracted so that only the fluctuating parts are considered. The data from all of the grid points constitute the data sample at each temporal instant, and a total of 201 realisations with the time interval of $\Delta t = 0.05$ are used to construct the ROM.

Notably, the inner product in the present POD is simply defined as

$$(\boldsymbol{v}_i, \boldsymbol{v}_j) = \sum_{n=1}^{M} (u_{ni}u_{nj} + v_{ni}v_{nj} + w_{ni}w_{nj} + \rho_{ni}\rho_{nj} + T_{ni}T_{nj}). \tag{3.1}$$

Therefore, the term POD 'energy', used for brevity in the following discussion, refers to the Euclid norm of the vector instead of the real physical energy. As pointed out in § 1, the definition of the inner product is one of the most important problems in ROM. Rowley *et al.* (2004) and Kalashnikova & Barone (2010) suggested that the inner product must satisfy the definition of total energy, to ensure that the projection of the modes on the governing equations is physically reasonable. Although the proposed data-driven method here has no need of governing equations, the results may still be dependent on the definition of the inner product. Because this paper focuses on the data-driven method itself, and this method can be used with any definition of the inner product, we will not further discuss the form of the inner product.

Following the algorithm described in § 2, the method will be explained in detail using the results of each step in ROM construction.

SVD is performed on the data sample matrix to obtain the POD modes and their energies, which are represented by the eigenvalues in (2.4). The total energy loss of the first i modes is defined as

$$El_i = \left(1 - \sum_{j=1}^{i} \sigma_j \Big/ \sum_{j=1}^{N} \sigma_j\right) \times 100\,\%. \tag{3.2}$$

As shown in figure 3, the first five modes are much higher in energy than the others, and together account for more than 95 % of the total energy. This indicates that these modes are sufficient to construct the ROM. The distributions of the streamwise disturbance velocity u of mode 2 and mode 4 on the plane at $y = 0.01$ are shown in figure 4. Mode 2 is clearly an H-type disturbance, while mode 4 is a K-type disturbance (Sayadi *et al.* 2014).

Next, DMD is applied. In figure 5(*a*), the eigenvalues of matrix $\boldsymbol{A}'$ are shown, coloured by the initial amplitudes of the modes. The SP algorithm is performed to obtain the important modes, marked with magenta circles. All of the eigenvalues lie either on or inside the unit circle, indicating that all of the modes are either neutrally stable or decay with time. The DMD frequency spectrum is shown in figure 5(*b*). The selected modes are shown with solid circles, and the corresponding frequencies are 3.9275 and 7.8559, which are the same as those of the disturbance introduced at the

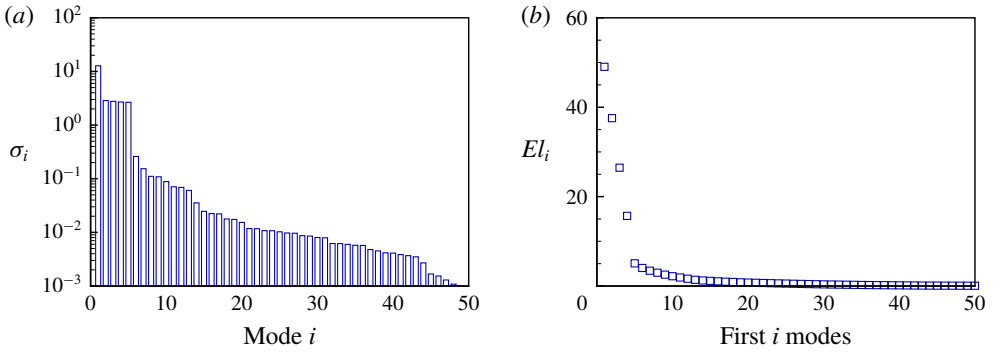

FIGURE 3. (Colour online) Energy of POD modes (*a*) and total energy loss of the first i modes (*b*).

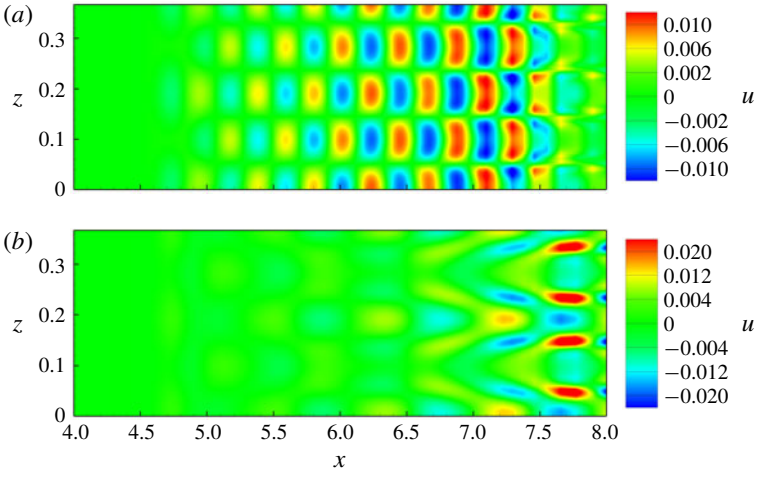

FIGURE 4. (Colour online) Contours of u of mode 2 (*a*) and mode 4 (*b*) on plane at $y = 0.01$.

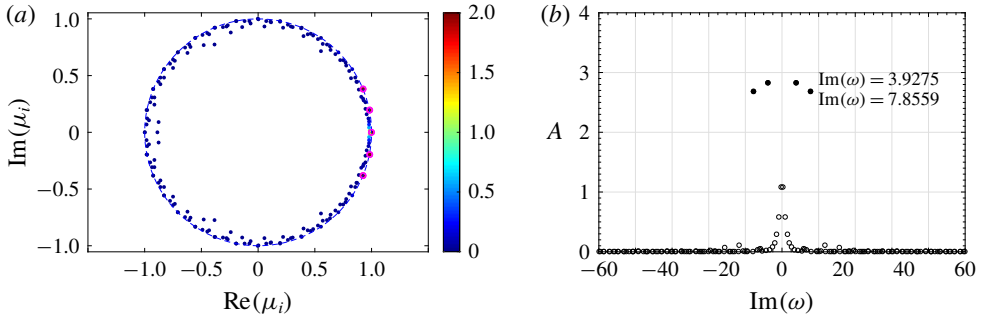

FIGURE 5. (Colour online) DMD eigenvalues (*a*) and spectrum (*b*); magenta circles in (*a*) and solid circles in (*b*) are modes selected by SP algorithm.

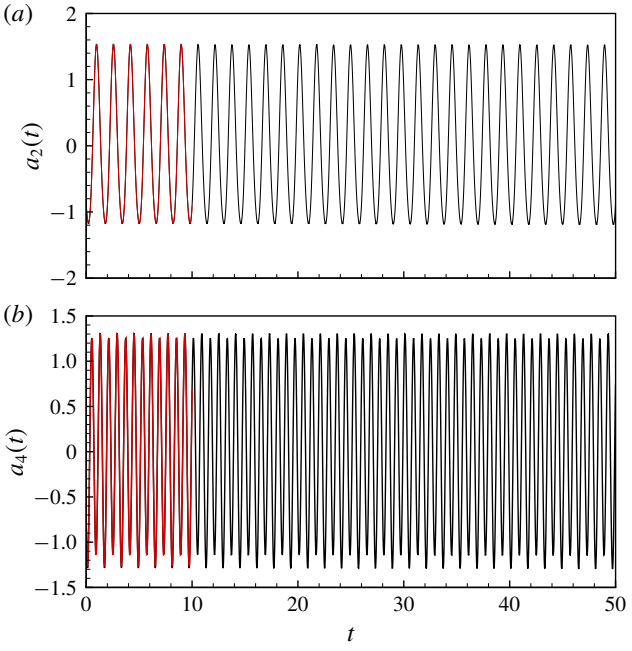

FIGURE 6. (Colour online) Temporal coefficients of mode 2 (*a*) and mode 4 (*b*): red, projected DNS data; black, ROM.

wall. The non-oscillating mode with the highest energy is not shown in figure 5(*b*) because it corresponds to the average flow field. The amplitudes of the selected modes are much higher than the others.

With the POD and DMD results above, the evolution matrix for the temporal coefficients of the POD modes can be easily obtained. The ODEs for the temporal evolution are solved with the fourth-order Runge–Kutta algorithm. The original DNS data are projected on the POD modes to obtain the initial values and the temporal coefficients of each mode for comparison. Because the oscillating POD modes come in pairs with different initial phases, only mode 2 and mode 4 are shown in figure 6. The temporal coefficients predicted by the ODEs agree very well with the projected DNS data within the time range used in POD. Because these modes are temporally stable and periodically evolving, the long-term evolution of the temporal coefficients should also be so. Therefore, the ROM accurately predicts the temporal evolution of the POD modes.

3.3. *Reduced-order model of bypass transition*

The ability of the ROM constructed above to accurately predict the temporal evolution of the POD modes is not surprising, because the flow field analysed above is linear, and the DMD, on which the present ROM construction method is based, assumes linear mapping. The method needs to be further tested by assessing its applicability to nonlinear flows. The computational parameters for the nonlinear case are listed in table 1. Compared with the linear case, the domain is longer streamwise and finer grids are used, to ensure that the entire transitional process can be accurately captured.

The flow quantities used in constructing the ROM are the same as those in the linear case. The time interval is $\Delta t = 0.02$ and a total of 201 temporal samples are included.

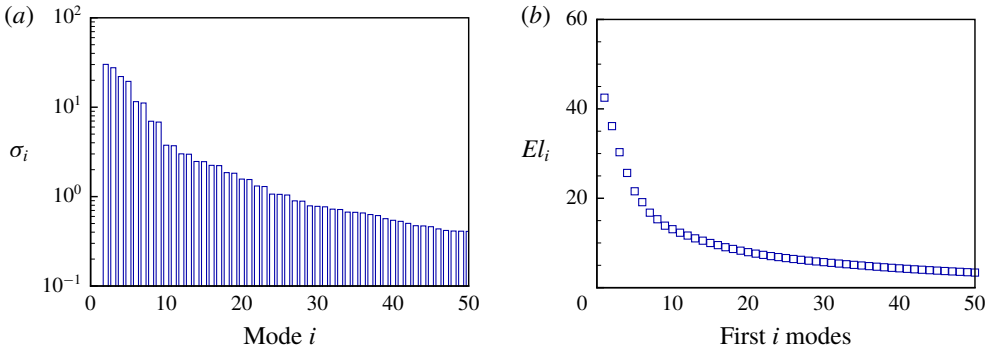

FIGURE 7. (Colour online) Energy of POD modes (*a*) and total energy loss of the first i modes (*b*).

The subzone in the range of $x = 5.0$–6.5 is selected for analysis because $x = 6.5$ marks the beginning of the transition (as shown in figure 2*b*), and the nonlinear effects in this region are obvious.

The energy of the POD modes and the total energy loss of the first i modes are shown in figure 7. The energy decreases slowly with increasing mode number, indicating the existence of complicated flow structures in the field caused by nonlinear effects. If the ROM is to capture 90 % of the total energy, 13 modes are needed, as shown in figure 7(*b*).

The vortical structures of the first four POD modes with the highest energy are shown in figure 8 as the isosurfaces of Q, the second invariant of the velocity gradient tensor. The structures are mainly streamwise-elongated vortices. They become stronger downstream, where the velocity disturbances around the vortices are more significant, as indicated by the contours of the streamwise disturbance velocity u. With increasing mode number (decreasing mode energy), the streamwise vortices become smaller and appear further downstream.

The DMD eigenvalues are shown in figure 9(*a*), coloured by the initial amplitude of the modes. The SP algorithm is then applied, and the modes selected are shown with magenta circles. The eigenvalues of the selected modes lie on the unit circle, indicating that the structures in these modes are neutrally stable. The DMD frequency spectrum is shown in figure 9(*b*), where the modes selected by the SP algorithm are shown with solid circles. The spectrum is more scattered and widely distributed as compared with the linear case. The low-frequency modes are higher in energy than the high-frequency modes. The results of the SP algorithm indicate that 19 modes are needed to capture the most important structures in the flow field. The total energy loss of the first i DMD modes is also investigated. As shown in figure 9(*c*), 19 modes are sufficient to capture 88 % of the total energy.

To examine the influence of the number of modes, we select 11, 15 and 21 modes, respectively, to construct the ROMs. (Note that the mode number provided by the SP algorithm is used as a reference, not a criterion, so we do not need to check whether 19 is the precise number of modes needed to establish an accurate and suitable ROM.) The temporal coefficients for each mode are obtained by solving (2.25) with the same numerical method as in the linear case. The results are compared with the projected DNS data, as shown in figure 10. The red symbols represent the projected DNS data in the time range where POD and DMD are performed (hereinafter referred to as the

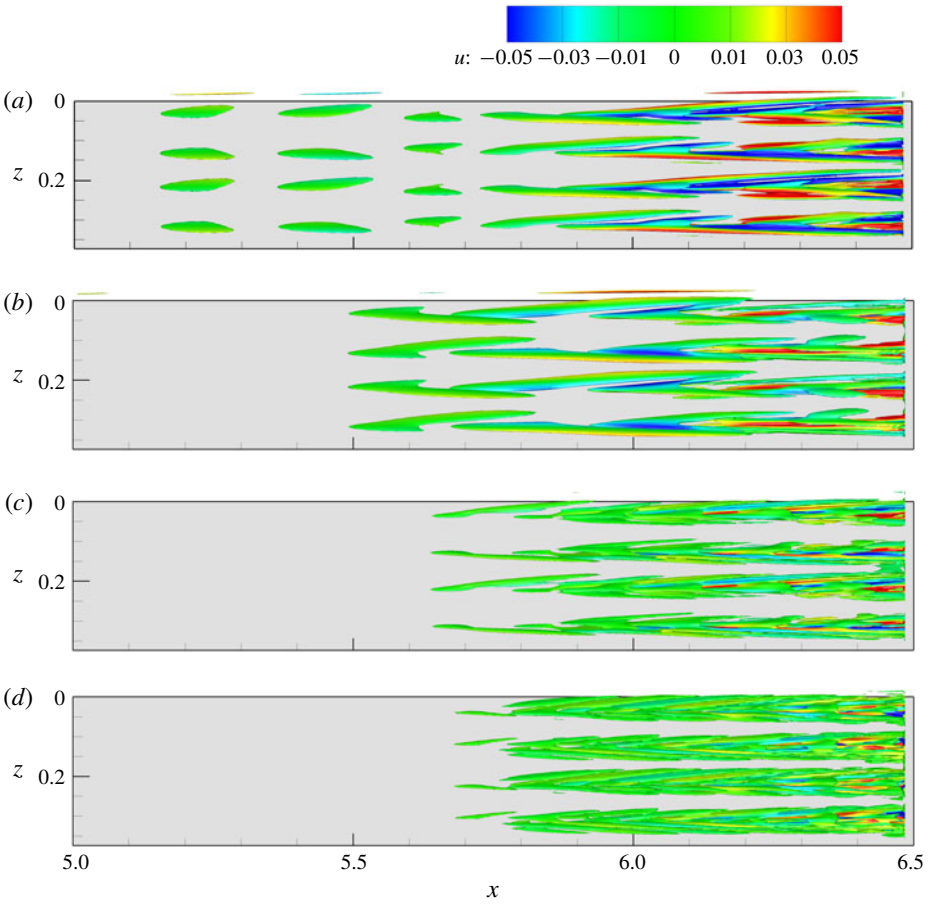

FIGURE 8. (Colour online) Isosurfaces of $Q = 0.0001$ coloured by u: (*a–d*) modes 2, 4, 6 and 8, respectively.

TRI), and the green symbols represent those beyond the TRI (hereinafter referred to as the TRO). For the temporal evolution of the lower modes 2–8, all of the ROMs yield accurate predictions both in the TRI and TRO. However, for mode 10, an obvious discrepancy can be observed between the result predicted by the ROM with 11 modes and the DNS data. Increasing the number of modes included in the ROM enhances the accuracy for mode 10, as shown by figure 10(II-*e*) and (III-*e*).

To quantify the prediction error of the ROMs, we define the averaged relative error as follows:

$$\mathrm{err}(t) = \frac{\left(\sum_{i=1}^{N} |a_i(t) - a_{pi}(t)|^2 / N\right)^{1/2}}{\left(\sum_{i=1}^{N} a_{pi}(t)^2\right)^{1/2}}, \tag{3.3}$$

where N is the number of modes, and a_{pi} represents the projected DNS data on POD mode i. As shown in figure 11, the relative error is less than 3 % in all cases,

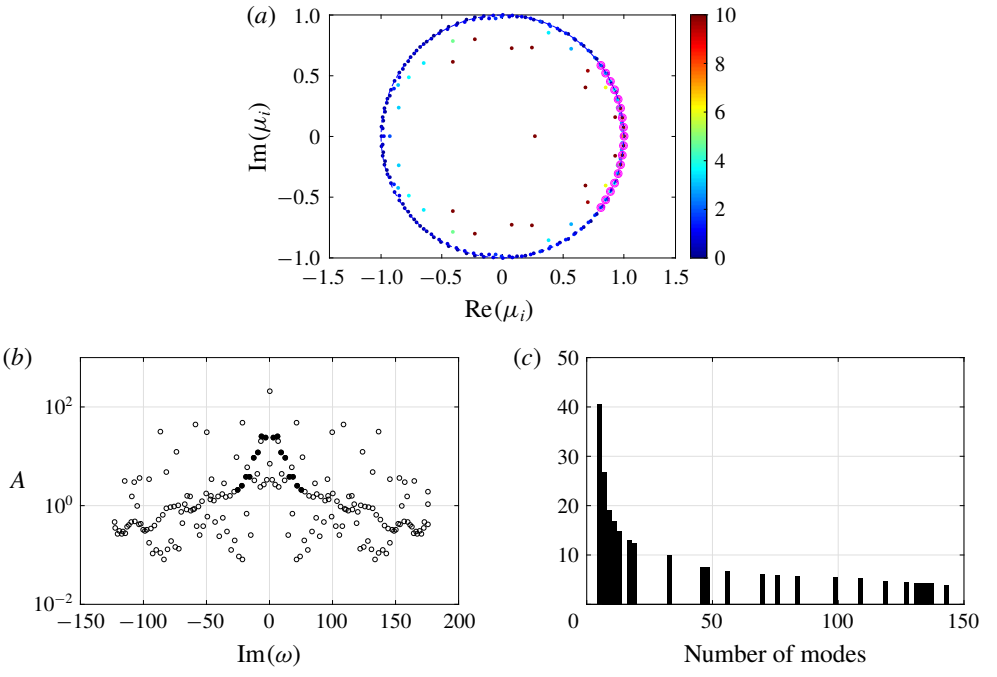

FIGURE 9. (Colour online) DMD eigenvalues (*a*), DMD frequency spectrum (*b*) and energy loss (%) as a function of the number of modes (*c*); magenta circles in (*a*) and solid circles in (*b*) are modes selected by SP algorithm.

and generally decreases when more modes are used in the ROMs. Notably, however, the relative error with 15 modes is larger than that with 11 modes at some temporal instants, especially near the peaks and in the TRO region. This is caused by the inaccurate prediction of the higher modes as discussed above.

Flow reconstruction is performed to further verify the ROMs. The temporally evolving POD modes are added together to obtain the predicted flow fields. The streamwise velocity u given by the ROMs with 11, 15 and 21 modes is compared with the original DNS data at four selected points at $x = 5.275$, 5.542, 5.803 and 6.058, $y = 0.01$, $z = 0.175$ inside the boundary layer. As shown in figure 12(I-*a*) to (I-*d*) for the ROM with 11 modes, the velocity u at $x = 5.275$, 5.542 and 5.803 can be accurately predicted, while further downstream at $x = 6.058$, where the transition is about to take place, the discrepancy is obvious between the predicted and DNS data. This suggests that in the transition region the nonlinear effects become stronger and the flow more complex, and more modes are needed to construct a ROM capable of sufficiently accurate prediction. Increasing the modes used to 15 and 21, the prediction at $x = 6.058$ becomes more accurate, as seen in figure 12(II-*d*) and (III-*d*). Besides the streamwise velocity u, the other flow quantities (not shown here) behave similarly. Thus, the reconstructed flow field confirms the accuracy of the ROMs.

The prediction error is also computed for the reconstructed u at $x = 6.058$, defined as

$$\mathrm{err}_2(t) = \frac{\left| u(t) - \sum_i^N b_i(t) u_i \right|}{u_{rms}} \times 100\,\%. \tag{3.4}$$

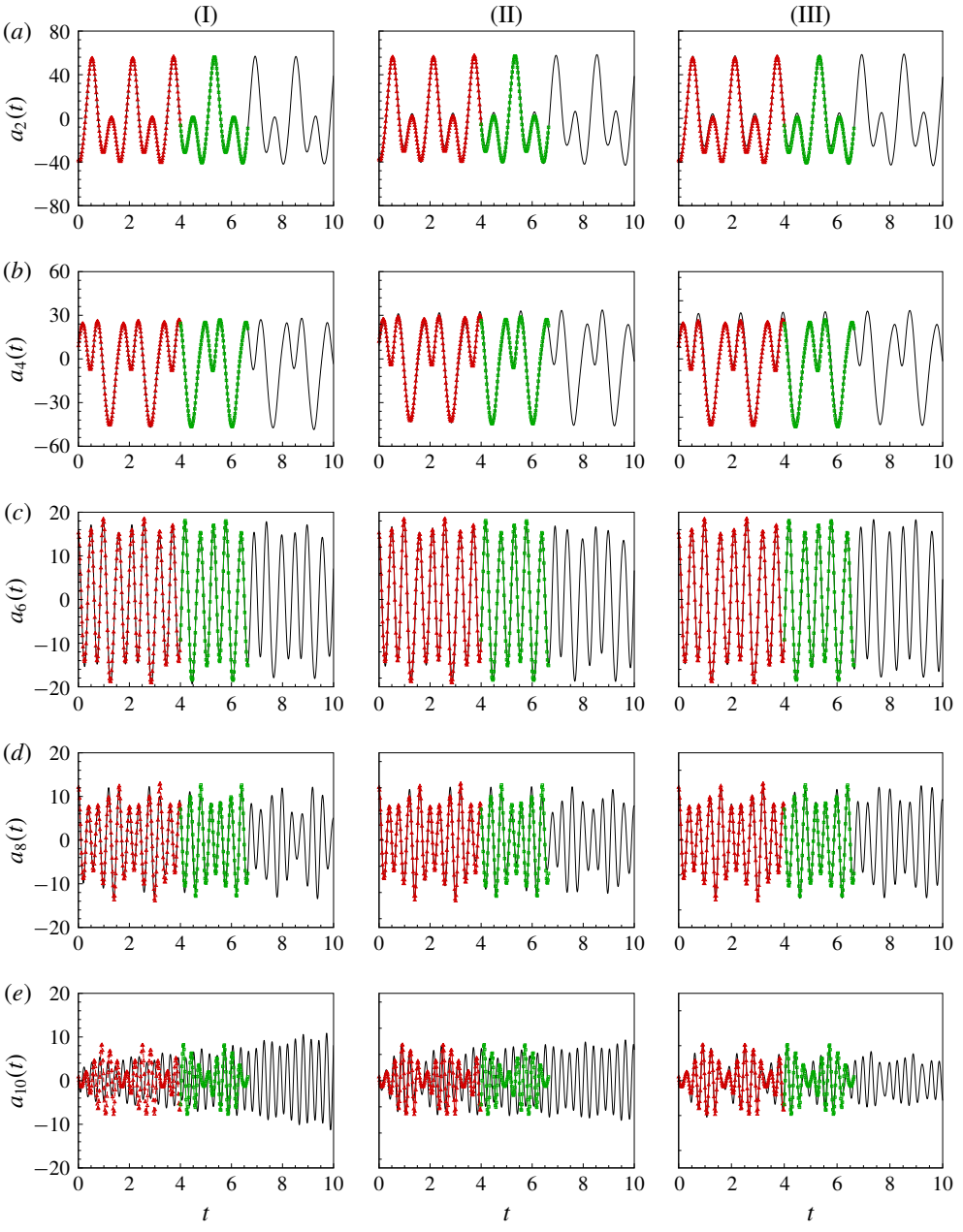

FIGURE 10. (Colour online) Temporal coefficients of mode 2, mode 4, mode 6, mode 8 and mode 10 (*a–e*) given by ROMs with 11, 15 and 21 modes (I–III): —△—, TRI; —□—, TRO; ——, ROM.

The results are shown in figure 13. The relative errors in the TRI for the three ROMs are small enough to be neglected. For the 11-mode ROM, the prediction error rises rapidly in the TRO, indicating that the ROM is unstable there. When the mode number in the ROM increases to 15 and 21, the error is reduced to below 2 %.

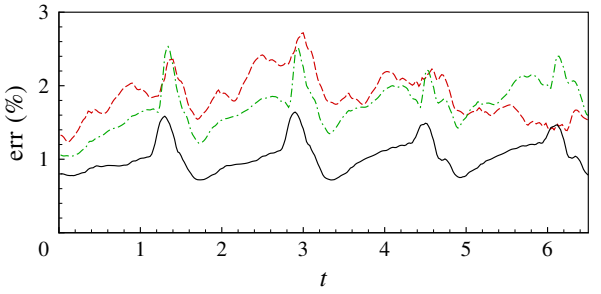

FIGURE 11. (Colour online) Errors of ROMs: red dashed line, 11 modes; green dashed-dotted line, 15 modes; black solid line, 21 modes.

11 modes	15 modes	21 modes
2.09×10^{-3}	9.86×10^{-4}	3.14×10^{-4}

TABLE 2. Largest amplification rates of the ROMs.

The stability of the ROMs can be determined from the real component of the eigenvalues of their temporal evolution matrix, which is referred to as the amplification rate in the following. The eigenvalues of the 11-, 15- and 21-mode ROMs considered herein were calculated and the largest amplification rates are listed in table 2. All of the eigenvalues are positive, indicating that all three ROMs are unstable. However, the largest amplification rate decreases as the order (number of modes) increases. Hence, although the absolute stability of the truncated ROMs cannot be guaranteed, increasing their order reduces the prediction error and prolongs the time period in which valid predictions can be made, as shown by figure 3 and table 2.

It is instructive to discuss the CPU times needed to obtain the ROMs and the computational savings of using this model. The computational time in this study includes solving the DNS, POD and DMD equations and the temporal evolution ODEs for the ROM. The cost of the first three procedures is independent of ROM size, while the last requires relatively little CPU time. An estimation of the CPU time costs for each procedure is listed below:

(i) CPU information: Intel(R) Xeon(R) CPU E5-2683 v3 @ 2.00 GHz.
(ii) DNS: approximately 15 CPU seconds multiplied by 24 cores per time step.
(iii) POD and DMD: approximately 9000 CPU seconds.
(iv) ROM (less than 30 modes): less than 6.0 CPU seconds for 100 000 steps.

To simulate 10 000 time steps, DNS would cost 3.6 million CPU seconds. However, for the ROM, the CPU time cost would be only 9000 CPU seconds for the POD and DMD procedures combined, which is much lower than that of DNS.

4. Concluding remarks and future work

In this paper, we propose a data-driven method to construct ROMs for complex flows. The method uses the POD modes as the orthogonal basis and obtains the time evolution ODEs by DMD. Being purely data-driven, this ROM construction method

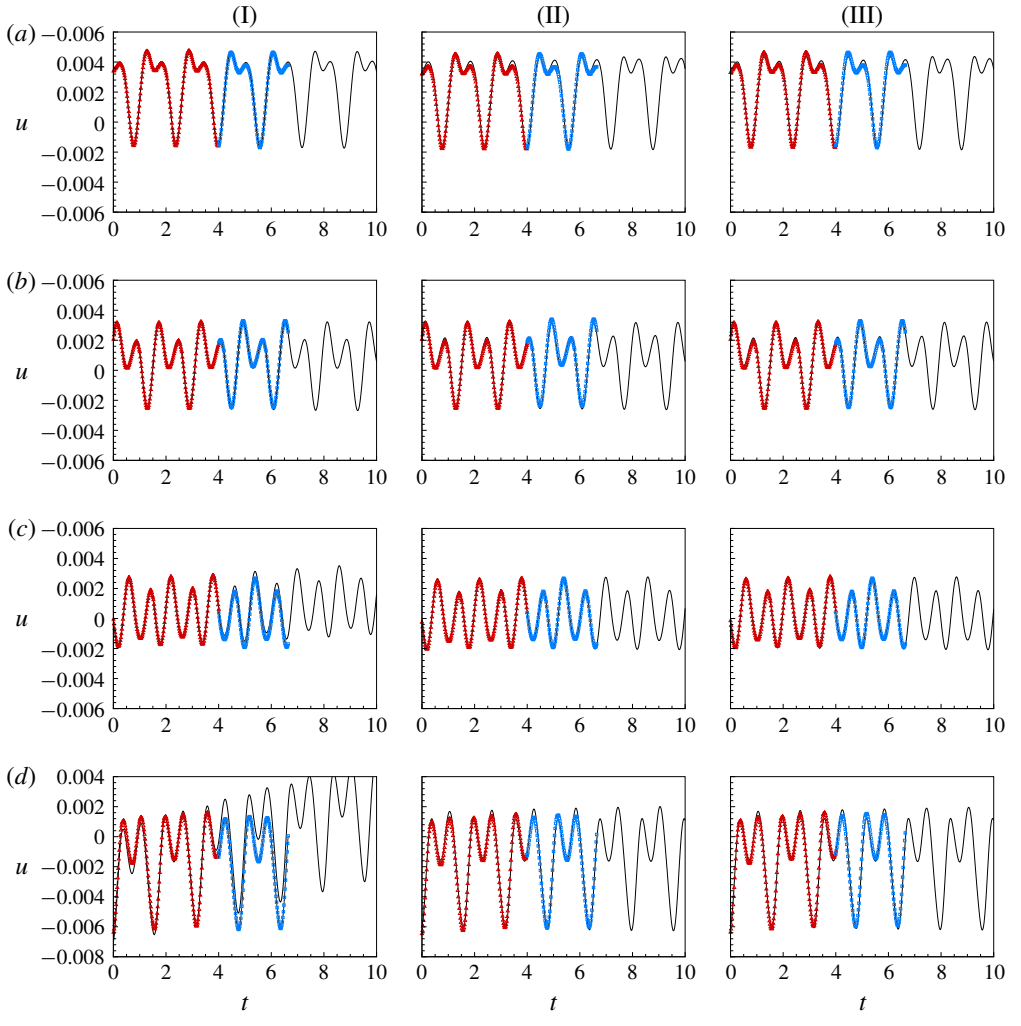

FIGURE 12. (Colour online) Time evolution of streamwise velocity u given by ROMs with 11, 15 and 21 modes (I–III) at $x = 5.275$, 5.542, 5.803 and 6.058, $y = 0.01$, $z = 0.175$ (*a–d*), respectively: —△—, TRI; —□—, TRO; ——, ROM.

can be easily applied to flows governed by complex equations such as compressible flows.

The ROMs of the natural and bypass transitions induced by linear and nonlinear disturbances in a supersonic boundary layer at $Ma = 2.25$ were built using the proposed method. The temporal coefficients of the POD modes and the reconstructed flow fields given by the ROMs were compared with those given by DNS data, confirming the practicality and accuracy of the present method. The influence of ROM dimensionality on the predicted flow was further examined by tracking the time history of the streamwise velocity u at different streamwise locations inside the boundary layer in the bypass transition case. It was found that, at downstream locations near the transition region, more modes were needed to give a satisfactory prediction because of the intensely complex flow.

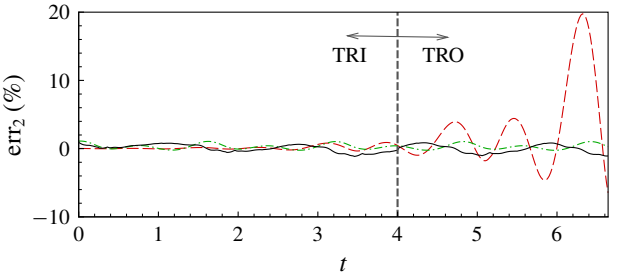

FIGURE 13. (Colour online) Errors of ROMs for the reconstructed u at $x = 6.058$: red dashed line, ROM with 11 modes; green dashed-dotted line, ROM with 15 modes; black solid line, ROM with 21 modes.

The present method was also applied to the bypass transition of a hypersonic boundary layer at $Ma = 6$ (not shown here). However, because the disturbance frequencies differ by several orders in hypersonic flow, data samples with a longer time span and finer time interval are needed. Owing to limited computational resources, the ROMs obtained herein can only accurately predict short-term behaviour. A promising approach to streamline the present ROM construction method is the multi-resolution DMD method proposed by Kutz, Fu & Brunton (2016), which we are now studying in our research.

Acknowledgements

This work was supported by the National Key Research and Development Programme of China (grant no. 2016YFA0401200) and the National Natural Science Foundation of China (grant no. 91752205).

REFERENCES

BALAJEWICZ, M., TEZAUR, I. & DOWELL, E. 2016 Minimal subspace rotation on the Stiefel manifold for stabilization and enhancement of projection-based reduced order models for the compressible Navier–Stokes equations. *J. Comput. Phys.* **321**, 224–241.

BARONE, M. F., KALASHNIKOVA, I., SEGALMAN, D. J. & THORNQUIST, H. K. 2009 Stable Galerkin reduced order models for linearized compressible flow. *J. Comput. Phys.* **228** (6), 1932–1946.

DURIEZ, T., BRUNTON, S. L. & NOACK, B. R. 2017 *Machine Learning Control – Taming Nonlinear Dynamics and Turbulence*. Springer International.

GLOERFELT, X. 2008 Compressible proper orthogonal decomposition/Galerkin reduced-order model of self-sustained oscillations in a cavity. *Phys. Fluids* **20** (11), 115105.

HOLMES, P., LUMLEY, J. L., BERKOOZ, G. & ROWLEY, C. W. 2012 *Turbulence, Coherent Structures, Dynamical Systems and Symmetry*. Cambridge University Press.

ILAK, M. & ROWLEY, C. W. 2008 Modeling of transitional channel flow using balanced proper orthogonal decomposition. *Phys. Fluids* **20** (3), 034103.

JOVANOVIĆ, M. R., SCHMID, P. J. & NICHOLS, J. W. 2014 Sparsity-promoting dynamic mode decomposition. *Phys. Fluids* **26** (2), 024103.

KALASHNIKOVA, I., ARUNAJATESAN, S., BARONE, M. F., VAN BLOEMEN WAANDERS, B. G. & FIKE, J. A. 2014*a* Reduced order modeling for prediction and control of large-scale systems. *Report, SAND*, (2014-4693). Sandia National Laboratories.

KALASHNIKOVA, I. & BARONE, M. F. 2010 On the stability and convergence of a Galerkin reduced order model (ROM) of compressible flow with solid wall and far-field boundary treatment. *Intl J. Numer. Meth. Engng* **83** (10), 1345–1375.

KALASHNIKOVA, I., BARONE, M. F., ARUNAJATESAN, S. & VAN BLOEMEN WAANDERS, B. G. 2014*b* Construction of energy-stable projection-based reduced order models. *Appl. Maths Comput.* **249**, 569–596.

KUTZ, J. N., FU, X. & BRUNTON, S. L. 2016 Multiresolution dynamic mode decomposition. *SIAM J. Appl. Dyn. Syst.* **15** (2), 713–735.

LI, X. L., FU, D. X., MA, Y. W. & LIANG, X. 2010 Direct numerical simulation of compressible turbulent flows. *Acta Mechanica Sin.* **26** (6), 795–806.

LUMLEY, J. L. & POJE, A. 1997 Low-dimensional models for flows with density fluctuations. *Phys. Fluids* **9** (7), 2023–2031.

NOACK, B. R., PAPAS, P. & MONKEWITZ, P. A. 2005 The need for a pressure-term representation in empirical Galerkin models of incompressible shear flows. *J. Fluid Mech.* **523**, 339–365.

NOACK, B. R., STANKIEWICZ, W., MORZYŃSKI, M. & SCHMID, P. J. 2016 Recursive dynamic mode decomposition of transient and post-transient wake flows. *J. Fluid Mech.* **809**, 843–872.

PIROZZOLI, S., GRASSO, F. & GATSKI, T. B. 2004 Direct numerical simulation and analysis of a spatially evolving supersonic turbulent boundary layer at $M = 2.25$. *Phys. Fluids* **16** (3), 530–545.

ROWLEY, C. W. 2005 Model reduction for fluids, using balanced proper orthogonal decomposition. *Intl J. Bifurcation Chaos* **15** (03), 997–1013.

ROWLEY, C. W., COLONIUS, T. & MURRAY, R. M. 2004 Model reduction for compressible flows using POD and Galerkin projection. *Physica* D*: Nonlinear Phenomena* **189** (1–2), 115–129.

ROWLEY, C. W. & DAWSON, S. T. 2017 Model reduction for flow analysis and control. *Annu. Rev. Fluid Mech.* **49**, 387–417.

SAYADI, T., SCHMID, P. J., NICHOLS, J. W. & MOIN, P. 2014 Reduced-order representation of near-wall structures in the late transitional boundary layer. *J. Fluid Mech.* **748**, 278–301.

SCHMID, P. J. 2010 Dynamic mode decomposition of numerical and experimental data. *J. Fluid Mech.* **656**, 5–28.

SMITH, T. R. 2003 Low-dimensional models of plane Couette flow using the proper orthogonal decomposition. PhD thesis, Princeton University.

SUBBAREDDY, P. K., BARTKOWICZ, M. D. & CANDLER, G. V. 2014 Direct numerical simulation of high-speed transition due to an isolated roughness element. *J. Fluid Mech.* **748**, 848–878.